JOURNAL OF SYNCHROTRON RADIATION
ISSN 1600-5775

Development of shock-dynamics study with synchrotron-based time-resolved X-ray diffraction using an Nd:glass laser system

Sota Takagi,[a,b]* Kouhei Ichiyanagi,[c,b] Atsushi Kyono,[a] Shunsuke Nozawa,[b] Nobuaki Kawai,[d] Ryo Fukaya,[b] Nobumasa Funamori[b] and Shin-ichi Adachi[b]

[a]Division of Earth Evolution Sciences, Graduate School of Life and Environmental Sciences, University of Tsukuba, 1-1-1 Tennodai, Tsukuba, Ibaraki 305-8572, Japan, [b]Institute of Materials Structure Science, High Energy Accelerator Research Organization (KEK), 1-1 Oho, Tsukuba, Ibaraki 305-0801, Japan, [c]Division of Biophysics, Department of Physiology, Jichi Medical University, 3311-1 Yakushiji, Shimotsuke, Tochigi 329-0498, Japan, and [d]Institute of Pulsed Power Science, Kumamoto University, 2-39-1 Kurokami, Kumamoto 860-8555, Japan.
*Correspondence e-mail: stakagi@geol.tsukuba.ac.jp

Received 23 August 2019
Accepted 29 November 2019

Edited by V. Favre-Nicolin, CEA and Université Joseph Fourier, France

Keywords: time-resolved X-ray diffraction; laser-induced shock; shock compression; deformation dynamics; crystallite fragmentation.

The combination of high-power laser and synchrotron X-ray pulses allows us to observe material responses under shock compression and release states at the crystal structure on a nanosecond time scale. A higher-power Nd:glass laser system for laser shock experiments was installed as a shock driving source at the NW14A beamline of PF-AR, KEK, Japan. It had a maximum pulse energy of 16 J, a pulse duration of 12 ns and a flat-top intensity profile on the target position. The shock-induced deformation dynamics of polycrystalline aluminium was investigated using synchrotron-based time-resolved X-ray diffraction (XRD) under laser-induced shock. The shock pressure reached up to about 17 GPa with a strain rate of at least 4.6×10^7 s^{-1} and remained there for nanoseconds. The plastic deformation caused by the shock-wave loading led to crystallite fragmentation. The preferred orientation of the polycrystalline aluminium remained essentially unchanged during the shock compression and release processes in this strain rate. The newly established time-resolved XRD experimental system can provide useful information for understanding the complex dynamic compression and release behaviors.

1. Introduction

Shock-wave compression of various condensed matter has long been a subject in fundamental solid-state physics, and therefore a number of shock-compression experiments have been performed to study the diverse phenomena of shock-compression states. The pressure and volume of bulk information under shock-wave loading have been obtained by wave-profile measurement using the VISAR (velocity interferometer system for any reflector). From the measurements, the Hugoniot elastic limit (HEL), plastic deformation characteristics, shock viscosity and phase transition pressure of shocked materials have been determined (McQueen *et al.*, 1967; Barker & Hollenbach, 1974; Swegle & Grady, 1985; Grady, 1998). In contrast, the microstructures of shocked materials have mainly been investigated by transmission electron analysis of the recovered samples (Gray & Huang, 1991; Meyers *et al.*, 2003). Since the structural dynamics of shock compression are essentially associated with the strain rate, the full understanding of the inherent structural dynamic behaviors of shocked materials requires the combination of two techniques, *i.e.* microscopic observation and real-time observation techniques.

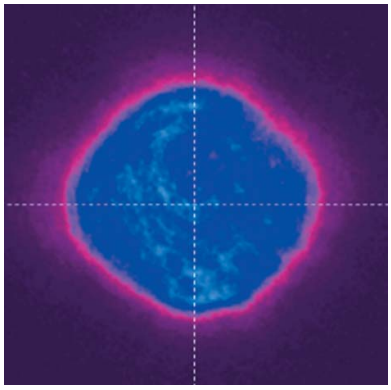

Recently, the *in situ* probing of dynamic behavior in shock-compressed materials has been extensively carried out using laser-plasma-based X-rays (*e.g.* Suggit *et al.*, 2010), synchrotron X-rays (*e.g.* Ichiyanagi *et al.*, 2007) and X-ray free-electron lasers (*e.g.* Milathianaki *et al.*, 2013). These techniques allow us to investigate the dynamic behaviors under shock-wave loading such as lattice evolutions around the HEL (Milathianaki *et al.*, 2013); phase-transition processes (Kalantar *et al.*, 2005; Hawreliak *et al.*, 2011; Rygg *et al.*, 2012; Coppari *et al.*, 2013; Gleason *et al.*, 2015; Torchio *et al.*, 2016; Denoeud *et al.*, 2016; Briggs *et al.*, 2017, 2019; Tracy *et al.*, 2018; Gorman *et al.*, 2018; Ichiyanagi *et al.*, 2019); plastic deformation processes including twinning, dislocation slips and grain refinement (Suggit *et al.*, 2012; Wehrenberg *et al.*, 2017; Sliwa *et al.*, 2018; Turneaure *et al.*, 2018); and phase-separation processes (Kraus *et al.*, 2017). (Quasi-)monochromatic and white-light X-rays have been used depending on the needs of the experiment. Comparing these two X-rays, the former are suitable for measuring strain profiles, long-range-ordered structures and the texture of polycrystalline samples, while the latter are suitable for determining unit-cell shapes with Laue diffraction and atomic-level dynamics with X-ray absorption fine-structure measurements (Torchio *et al.*, 2016; Niwa *et al.*, 2016). From this point of view, synchrotron X-ray sources have a great advantage over other X-ray sources because the wavelength and energy bandwidth can be continuously varied.

The Photon Factory Advanced Ring (PF-AR), High Energy Accelerator Research Organization (KEK), Japan, is operated with a single-bunch mode in a 6.5 GeV ring and has thus enabled us to perform snapshot-type time-resolved measurements. For the shock experiments, our group previously performed time-resolved X-ray diffraction (XRD) measurements at a pressure of less than 10 GPa at the NW14A beamline (Ichiyanagi *et al.*, 2007, 2012; Hu *et al.*, 2012, 2013). The dynamic behaviors of crystals, polycrystals and amorphous materials under shock conditions were studied by combining a nanosecond-pulse laser and a high-flux X-ray source with a 1–15% energy bandwidth (Ichiyanagi & Nakamura, 2016). To measure the wide range of dynamics above the elastic limits of materials, it is necessary to increase the laser power with a flat-top spatial distribution. In this study, we installed a higher-power Nd:glass laser system as a shock driving source at the NW14A beamline and measured the deformation dynamics of polycrystalline aluminium with a synchrotron-based time-resolved XRD system under shock loading. Here, we briefly report the features of this system and present the results of shock experiments where the samples were shocked at pressures of up to at least 17 GPa.

2. Laser and X-ray system

The customized high-power Nd:glass laser (NG 450, Amplitude Laser Group) was installed in the experimental hutch at the NW14A beamline at the PF-AR. The Nd:glass laser system combined with the time-resolved XRD system is shown in Fig. 1(*a*). The laser system was composed of an oscillator system (Q-switch Nd:YAG laser) and three Nd:glass amplifiers (9 mm-, 16 mm- and 25 mm-diameter rods). The Nd:YAG laser pulses were emitted at 9.46 Hz. The timing jitter of the laser pulses was less than 1 ns. The timing synchronization of the laser pulses and synchrotron X-ray pulses is described later. One laser pulse was amplified by a first-stage (9 mm diameter) glass laser and isolated by a laser shutter. The laser pulse was further amplified by second- and third-stage glass lasers (16 mm and 25 mm diameter) to a maximum energy of 16 J. Because of the cooling time of the three Nd:glass amplifier rods, the repetition time was 20 min shot^{-1}. The wavelength and pulse width at full width at half-maximum (FWHM) were 1064 nm and 12 ns, respectively. A vacuum spatial filter (VSF) in the laser path was placed between the 9 mm- and 16 mm-diameter amplifiers. An aperture was placed after the VSF to obtain a steep edge of the spatial profile. The amplified beam was focused using a focus lens with a 150 mm focal length. A flat-top beam image was

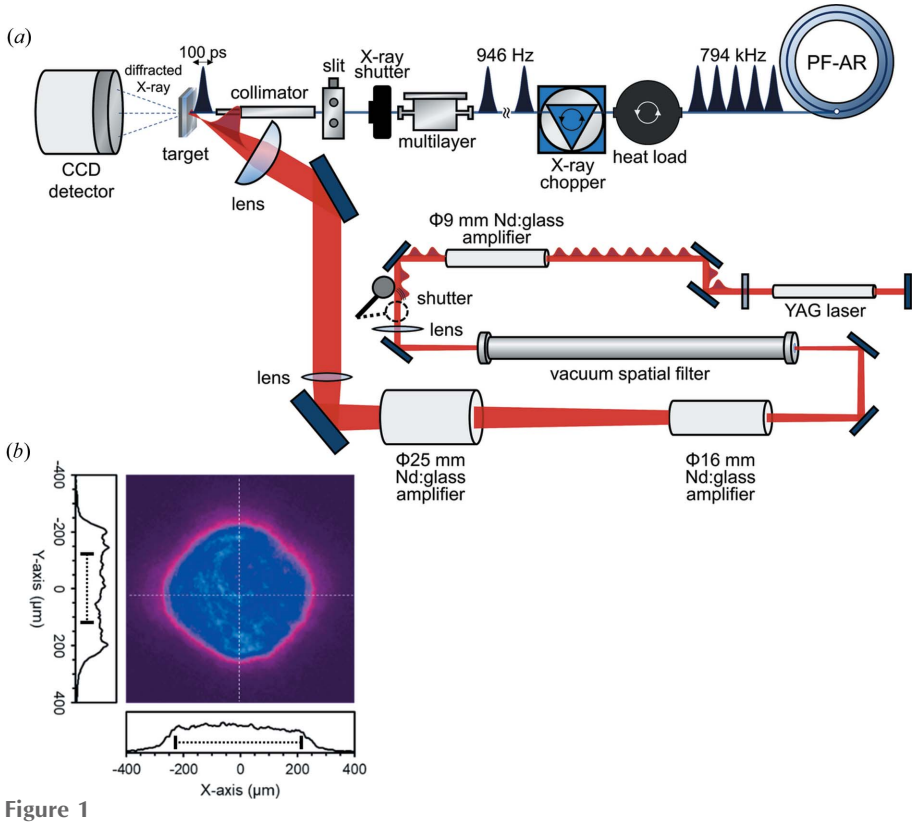

Figure 1
(*a*) Schematic of the Nd:glass laser system with the time-resolved XRD system. (*b*) Laser-beam profile at the target position. The dotted lines represent the X-ray beam size (FWHM).

obtained by amplifying the oscillator beam with a Gaussian spatial intensity profile. It was imaged by defocusing the lens. Fig. 1(*b*) shows the laser-beam profile measured by the charge-coupled device (CCD) camera (SP620U, Ophir Photonics) at the target position. The sample chamber including the sample and the lens was vacuumed to <1 Pa to avoid laser-induced air breakdown around the focus point.

An X-ray pulse was obtained through the U20 undulator. Details of the X-ray optics in the NW14A beamline have been described by Nozawa *et al.* (2007). A white-light X-ray ($\Delta E/E \simeq 15\%$) can be obtained with the default setup of the beamline. Quasi-monochromatic ($\Delta E/E \simeq 1.5\%$) X-rays can also be obtained using W/B_4C multilayer X-ray optics (Ichiyanagi *et al.*, 2009). The pulse duration was about 100 ps. The beam size at the sample position was 460 µm (H) × 240 µm (V) FWHM.

The timing chart of the time-resolved XRD measurement system is illustrated in Fig. 2. The synchronization of the timing was based on a radiofrequency (RF) master clock, 508 MHz, of the PF-AR storage ring. In the X-ray isolation system, 946 Hz X-ray pulses were isolated from 794 kHz by a water-cooled heat-load chopper and X-ray pulse selector (Forschungszentrum Jülich). One X-ray pulse was finally extracted from the 946 Hz pulsed X-ray by a solenoid X-ray shutter (XRS1S2P0, Uniblitz). In the laser system, on the other hand, the 9.46 Hz repetition timing of the Nd:YAG laser was emitted from a frequency divider (T3687-01, Tsuji Electronics Co. Ltd), which divided the 508 MHz RF master clock into 9.46 Hz. One laser pulse was then isolated by the laser shutter and the pulse was amplified by Nd:glass amplifiers. Once the measurement program was triggered, the flash lamps of the amplifiers were charged at the first signal on the 9.46 Hz clock. Because the flash lamp of the 25 mm-diameter amplifier required about 20 s to be charged, the flash lamp was discharged at intervals of 19.18 s. The gate signals of the X-ray shutter and the laser shutter were synchronized with the isolated X-ray pulse. The relative delay time between the laser and the X-ray pulses was controlled by delay generators (DG645, Stanford Research System, Inc.). The timing of the laser pulse compared with the X-ray pulse was measured using the transmitted amplified laser light by a high-speed InGaAs photodiode behind the mirror in the laser path. The target was replaced after each laser shot because it was damaged.

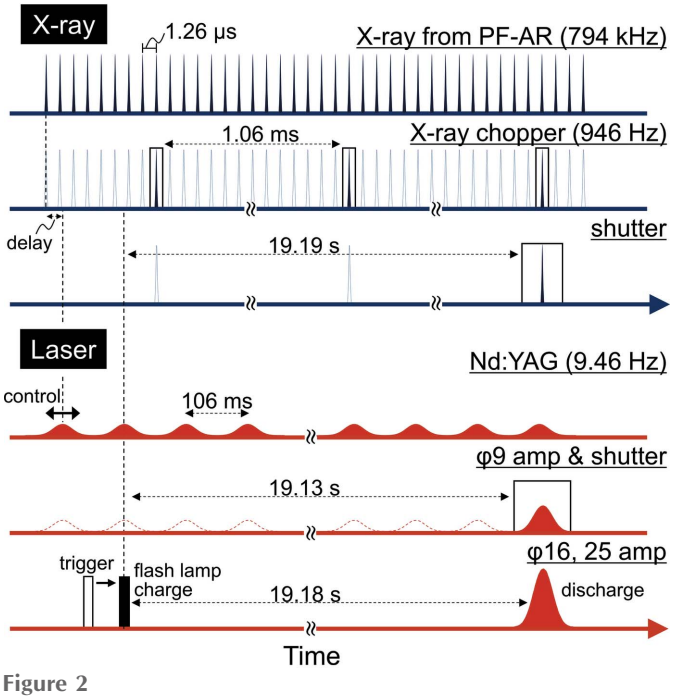

Figure 2
Timing chart of the synchronization system between the X-ray and the laser.

3. Experimental

Commercially available polycrystalline aluminium foils with thicknesses of 50 µm (purity ≥ 99%, Nilaco Co. Ltd) were used in this study. The aluminium crystallizes in the face-centered cubic (f.c.c.) structure with a lattice constant a = 4.051 (4) Å and space group $Fm\bar{3}m$ (No. 225) at ambient conditions. The mean grain size of the sample was ∼30 µm. A polyethylene terephthalate (PET) film of 25 µm thickness was attached as an ablator on the sample surface, which was further coated with a 40 nm aluminium layer (Fig. 3). The aluminium coating was used as a sacrificial layer, which cuts off the front tail of the laser time profile. This coating avoids generating a weak pre-shock wave. The spot diameter of the laser beam on the target surface was about 450 µm in the flat-top region. The laser intensity at the target surface was about 6.6×10^{11} W cm^{-2}. The ablator was converted into plasma by the laser beam. The compression wave in the sample was generated by an expanding plasma produced by the laser ablation of the PET film. The peak energy and energy bandwidth of the quasi-monochromated X-rays were 15.6 keV (λ = 0.797 Å) and $\Delta E/E$ = 1.53%, respectively. The XRD patterns were recorded in transmission geometry with an integrating CCD (MarCCD 165, Rayonix, LLC) consisting of 2048 × 2048 pixels with a 79.272 µm × 79.272 µm pixel size. The collected data were processed using the *Fit2d* program (Hammersley, 2016). The detector-geometry parameters were calibrated using the diffraction peaks of Si powder (purity ≥ 99%; Kojundo Chemical Laboratory Co. Ltd). The Debye–Scherrer

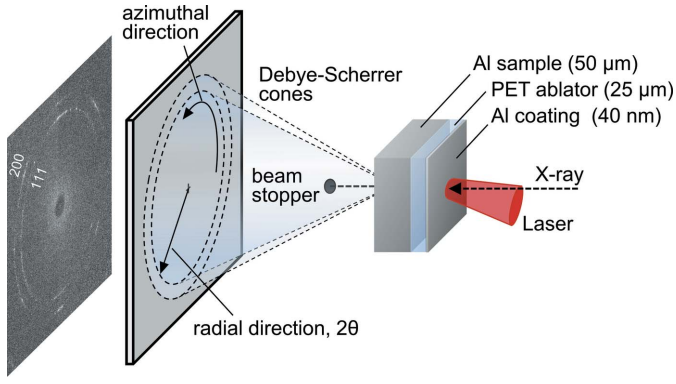

Figure 3
Schematic representation of target arrangement and XRD.

rings corresponding to the (111) and (200) crystallographic planes of aluminium were used to determine the orientation distribution function. Because of the experimental constraint, a single diffraction image was used to obtain a reconstructed pole figure. Each XRD image was separated into 72 sections along an azimuthal direction by 5° steps. Rietveld software *MAUD* (Lutterotti *et al.*, 1999*a*,*b*) and *BEARTEX* (Wenk *et al.*, 1998) were employed to calculate the reconstructed pole figures.

4. Results and discussion

4.1. Compression and release dynamics

Fig. 4 shows the azimuthally integrated time-resolved XRD profiles of the polycrystalline aluminium. Each XRD pattern was obtained by one X-ray pulse. Changes in the (111) and (200) diffraction patterns were continuously observed, which was attributed to the resulting states caused by the propagating shock wave followed by a rarefaction wave. At 2.9 ns, diffraction peaks derived from the shock-compressed (111) and (200) planes clearly appeared. The diffraction peaks around $2\theta = 19.61°$ and 22.71° are derived from the ambient phase, while those around $2\theta = 20.57°$ and 23.86° are from the compressed phase. In the experiment, since the laser-beam diameter was slightly smaller than the width of the X-ray beam the diffraction data from the ambient phase are always included. The diffraction peaks from the compressed phase appear at higher angles than those from the ambient phase, indicating a reduction in *d* spacing. The lattice constant under shock-compression timing was calculated from the measured *d* spacing at each delay timing. The *d* spacings of (111) and (200) and the lattice constant at the ambient and compressed states are summarized in Table 1. At each delay timing, the lattice constants calculated from the *d* spacings of (111) and (200) are almost identical, suggesting an isotropic compression state under the shock-wave loading. The compressibility of the unit-cell volume at 2.9 ns was calculated to be $\Delta V/V_0 = -13.4\%$, where V_0 and ΔV represent the initial volume and the change in the volume, respectively. The estimated strain rate at the shock front was at least 4.6×10^7 s^{-1} (= 0.134/2.9 ns). At 5.0 ns, diffraction peaks of shock-compressed aluminium were shifted further to higher angles. Compressibility was achieved at $\Delta V/V_0 = -14.3\%$. We calculated the shock pressure from the observation results using the equation of state of aluminium. The upper axes of Figs. 4(*a*) and 4(*b*) show the shock pressure estimated from the *d* spacing using the following equation of the Hugoniot relationship,

$$P_{\rm H} = \frac{\rho_0 C_0^2 \eta}{(1 - s\eta)^2},$$

where ρ_0 is the initial density, C_0 is the speed of sound in aluminium, *s* is the shock data parameter and η (= $1 - V/V_0$) is the compressive volumetric strain. The values of C_0 (= 5.389 km s^{-1}) and *s* (= 1.339) were quoted from the U_s–u_p relationship of aluminium (Mitchell & Nellis, 1981). As a result, the shock pressure reached up to at least 17 GPa. This estimated pressure is much higher than the HEL of pure aluminium, which was previously investigated using an aluminium thin film (Gupta *et al.*, 2009; Whitley *et al.*, 2011). No structural phase transition was observed under compressed state in this study, which is consistent with the result in the previous study (Nellis *et al.*, 1988). At 10.6 ns, the diffraction peaks from highly compressed aluminium disappeared, which indicated that the shock pressure was released by the rarefaction wave propagating back into the sample. Between 10.6 and 11.5 ns, both the (111) and (200) diffraction peaks shifted slightly to lower angles than their ambient positions, implying that a small volume expansion was induced by the release. The volume expansion, $\Delta V/V_0$, at 11.5 ns was about 1.8%. The expansion after shock compression, associated with the propagation of the rarefaction wave, has also been observed in the previous experimental work on laser-shocked tantalum (Albertazzi *et al.*, 2017). At 15.5 ns, the peak-top positions of the (111) and (200) diffraction peaks almost returned to ambient position. Further compression after the expansion did not appear in the time range of the present experiment, although it was observed by Albertazzi *et al.* (2017). Comparing between

Table 1
Observed *d* spacing at ambient conditions, 2.9 and 5.0 ns, and calculated lattice constant assuming isotropic compression.

	Ambient		2.9 ns		5.0 ns	
	d (Å)	*a* (Å)	*d* (Å)	*a* (Å)	*d* (Å)	*a* (Å)
(111)	2.340	4.053	2.232	3.865	2.220	3.846
(200)	2.024	4.048	1.928	3.856	1.926	3.852
$a_{\rm average}$		4.051 (4)		3.861 (7)		3.848 (5)

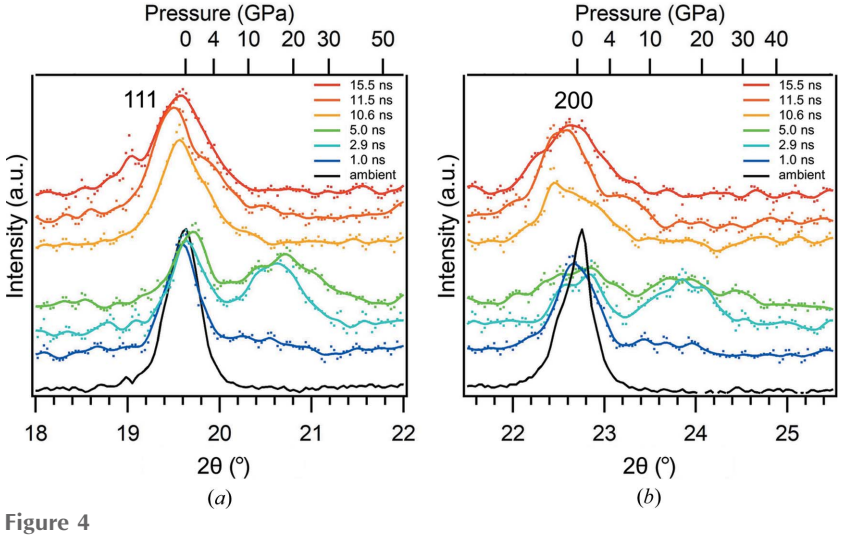

Figure 4
Time evolutions of (*a*) (111) and (*b*) (200) XRD peaks from polycrystalline aluminium. The dotted and solid lines indicate the observed and smoothed data, respectively.

diffraction patterns of ambient and 15.5 ns, the diffraction peaks broadened because of the crystallite fragmentation. This can also be explained by the change in diffraction signals from spotty to continuous rings, which is discussed in the next section.

4.2. *In situ* crystallite fragmentation

The information concerning *in situ* crystallite orientation distributions under shock-wave loading could be extracted from the Debye–Scherrer patterns. The 2D diffraction images for ambient, compressed (2.9 and 5.0 ns) and released states (11.5 and 15.5 ns) are shown in Fig. 5. They show clear Debye–Scherrer rings belonging to the (111) and (200) crystallographic planes of aluminium. The Debye–Scherrer rings with some spots and spotty rings [Fig. 5(*a*)] suggest that before the shock wave reached the sample surface there were relatively large crystallites in the X-ray beam irradiated region. For compression states (2.9 and 5.0 ns), the number of sharp diffraction spots decrease with the shock-wave propagation into the sample, while some broadened diffraction spots appear at the higher angle side with the increase in the shock-compressed region [Figs. 5(*b*) and 5(*c*)]. Moreover, a spreading of diffraction spots along the azimuthal direction implies that the crystallites further fragmented into smaller sizes by the compression wave. At 15.5 ns, the diffraction signals almost changed to a line [Fig. 5(*d*)]. The similar grain fragmentation behavior during the lower shock compression has also been observed on polycrystalline aluminium (Ichiyanagi *et al.*, 2019).

The most striking result is that the diffraction rings produced by the shock wave show the azimuthal variation of the intensity. Figs. 5(*e*) and 5(*f*) show the reconstructed {111} pole figures from the diffraction images obtained before the shock arrival [Fig. 5(*a*)] and at 15.5 ns [Fig. 5(*d*)]. The orientations along {110}⟨001⟩ are predominantly orientated in the sample. As can be seen, the preferred orientation remains essentially unchanged. The results indicate that, even when the grains of polycrystalline aluminium are fragmented into finer ones by the shock loading, the created subgrains have preferred orientations almost identical to the original sample. The direct measurements of microtexture, grain size and crystal structure change, using the high-power laser and single X-ray pulses, provide insight into the unique microstructural features of shock-compressed materials.

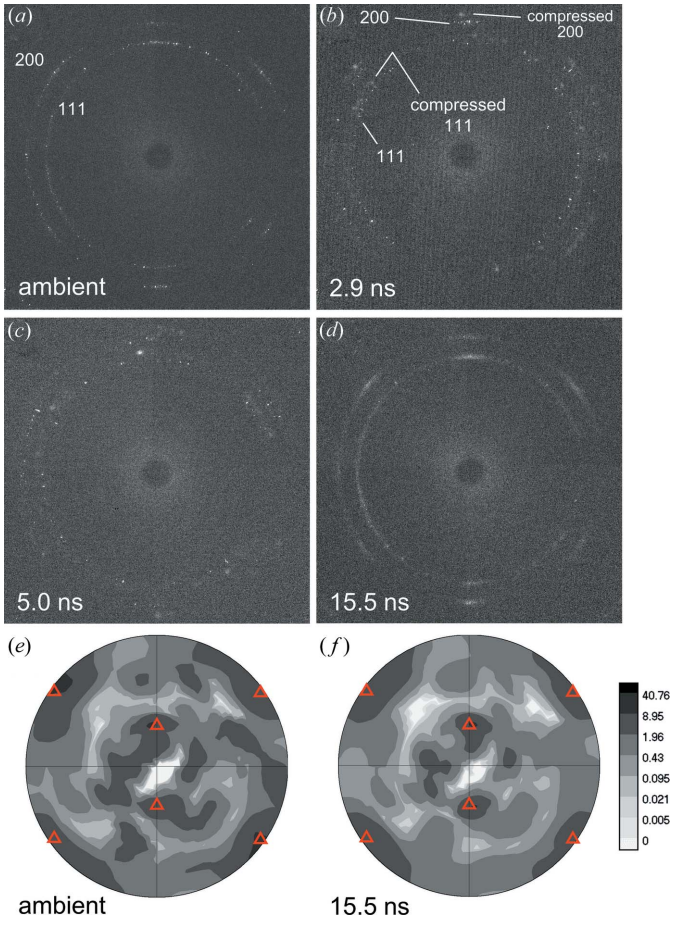

Figure 5
Time-resolved XRD images at (*a*) ambient, (*b*) 2.9, (*c*) 5.0 and (*d*) 15.5 ns. Reconstructed {111} pole figures at (*e*) ambient and (*f*) 15.5 ns. The red triangle represents {110}⟨001⟩.

5. Conclusions

A Nd:glass laser system was installed at the NW14A beamline, PF-AR, KEK, Japan, for a laser-shock experiment, with a maximum pulse energy of 16 J, a pulse duration of 12 ns and flat-top intensity profiles on the target. We developed a timing synchronization system for the laser and synchrotron X-ray pulses. The deformation dynamics of polycrystalline aluminium was measured using a time-resolved XRD method. The shock pressure reached up to about 17 GPa with a strain rate of at least 4.6×10^7 s^{-1} and remained there for nanoseconds. The time-resolved XRD patterns demonstrated that the spotty rings from the aluminium crystallites changed with the delay time into near-continuous rings. These changes indicate that the plastic deformation caused by shock-wave loading led to the crystallite fragmentation. Moreover, even during the shock compression and release processes the created subgrains had preferred orientations almost identical to the original sample. The established system can be applied to single-crystal Laue diffraction measurement by switching from monochromatic to white X-ray beams. The newly established time-resolved XRD experimental system can provide useful information for understanding the complex dynamic compression and release behaviors, which are still not well understood.

Acknowledgements

This work was performed under the approval of the Photon Factory Program Advisory Committee (Proposal No. 2015S2-006; 2017T-002). We thank K. G. Nakamura for transferring the Nd:glass laser system, which had been used at Tokyo Tech, to KEK PF-AR. We would like to thank Editage (https://www.editage.com) for English-language editing.

Funding information

This work was supported by a JSPS Grant-in-Aid for Young Scientists (A) (grant number JP17H04820), a JSPS Grant-in-Aid for Challenging Exploratory Research (grant number JP17K18999), a Grant-in-Aid for Scientific Research on Innovation Areas 'Soft Crystals' (Area 2903, grant number JP17H06372), a Grant-in-Aid for Scientific Research (C) (grant number JP17K05702) and a Grant-in-Aid for JSPS Research Fellows (grant number JP18J11126) from the Japan Society for the Promotion of Science (JSPS). Financial support was also provided by the Toray Science Foundation and the Amada Foundation.

References

Albertazzi, B., Ozaki, N., Zhakhovsky, V., Faenov, A., Habara, H., Harmand, M., Hartley, N., Ilnitsky, D., Inogamov, N., Inubushi, Y., Ishikawa, T., Katayama, T., Koyama, T., Koenig, M., Krygier, A., Matsuoka, T., Matsuyama, S., McBride, E., Migdal, K. P., Morard, G., Ohashi, H., Okuchi, T., Pikuz, T., Purevjav, N., Sakata, O., Sano, Y., Sato, T., Sekine, T., Seto, Y., Takahashi, K., Tanaka, K., Tange, Y., Togashi, T., Tono, K., Umeda, Y., Vinci, T., Yabashi, M., Yabuuchi, T., Yamauchi, K., Yumoto, H. & Kodama, R. (2017). *Sci. Adv.* **3**, e1602705.

Barker, L. M. & Hollenbach, R. E. (1974). *J. Appl. Phys.* **45**, 4872–4887.

Briggs, R., Gorman, M. G., Coleman, A. L., McWilliams, R. S., McBride, E. E., McGonegle, D., Wark, J. S., Peacock, L., Rothman, S., Macleod, S. G., Bolme, C. A., Gleason, A. E., Collins, G. W., Eggert, J. H., Fratanduono, D. E., Smith, R. F., Galtier, E., Granados, E., Lee, H. J., Nagler, B., Nam, I., Xing, Z. & McMahon, M. I. (2017). *Phys. Rev. Lett.* **118**, 025501.

Briggs, R., Torchio, R., Sollier, A., Occelli, F., Videau, L., Kretzschmar, N. & Wulff, M. (2019). *J. Synchrotron Rad.* **26**, 96–101.

Coppari, F., Smith, R. F., Eggert, J. H., Wang, J., Rygg, J. R., Lazicki, A., Hawreliak, J. A., Collins, G. W. & Duffy, T. S. (2013). *Nat. Geosci.* **6**, 926–929.

Denoeud, A., Ozaki, N., Benuzzi-Mounaix, A., Uranishi, H., Kondo, Y., Kodama, R., Brambrink, E., Ravasio, A., Bocoum, M., Boudenne, J. M., Harmand, M., Guyot, F., Mazevet, S., Riley, D., Makita, M., Sano, T., Sakawa, Y., Inubushi, Y., Gregori, G., Koenig, M. & Morard, G. (2016). *Proc. Natl Acad. Sci. USA*, **113**, 7745–7749.

Gleason, A. E., Bolme, C. A., Lee, H. J., Nagler, B., Galtier, E., Milathianaki, D., Hawreliak, J., Kraus, R. G., Eggert, J. H., Fratanduono, D. E., Collins, G. W., Sandberg, R., Yang, W. & Mao, W. L. (2015). *Nat. Commun.* **6**, 8191.

Gorman, M. G., Coleman, A. L., Briggs, R., McWilliams, R. S., McGonegle, D., Bolme, C. A., Gleason, A. E., Galtier, E., Lee, H. J., Granados, E., Śliwa, M., Sanloup, C., Rothman, S., Fratanduono, D. E., Smith, R. F., Collins, G. W., Eggert, J. H., Wark, J. S. & McMahon, M. I. (2018). *Sci. Rep.* **8**, 16927.

Grady, D. E. (1998). *Mech. Mater.* **29**, 181–203.

Gray, G. T. & Huang, J. C. (1991). *Mater. Sci. Eng. A*, **145**, 21–35.

Gupta, Y. M., Winey, J. M., Trivedi, P. B., LaLone, B. M., Smith, R. F., Eggert, J. H. & Collins, G. W. (2009). *J. Appl. Phys.* **105**, 036107.

Hammersley, A. P. (2016). *J. Appl. Cryst.* **49**, 646–652.

Hawreliak, J. A., El-Dasher, B., Lorenzana, H., Kimminau, G., Higginbotham, A., Nagler, B., Vinko, S. M., Murphy, W. J., Whitcher, T., Wark, J. S., Rothman, S. & Park, N. (2011). *Phys. Rev. B*, **83**, 144114.

Hu, J., Ichiyanagi, K., Takahashi, H., Koguchi, H., Akasaka, T., Kawai, N., Nozawa, S., Sato, T., Sasaki, Y. C., Adachi, S. & Nakamura, K. G. (2013). *J. Appl. Phys.* **113**, 039901.

Hu, J. B., Ichiyanagi, K., Takahashi, H., Koguchi, H., Akasaka, T., Kawai, N., Nozawa, S., Sato, T., Sasaki, Y. C., Adachi, S. & Nakamura, K. G. (2012). *J. Appl. Phys.* **111**, 053526.

Ichiyanagi, K., Adachi, S. I., Nozawa, S., Hironaka, Y., Nakamura, K. G., Sato, T., Tomita, A. & Koshihara, S. Y. (2007). *Appl. Phys. Lett.* **91**, 231918.

Ichiyanagi, K., Kawai, N., Nozawa, S., Sato, T., Tomita, A., Hoshino, M., Nakamura, K. G., Adachi, S. & Sasaki, Y. C. (2012). *Appl. Phys. Lett.* **101**, 181901.

Ichiyanagi, K. & Nakamura, K. G. (2016). *Metals*, **6**, 17.

Ichiyanagi, K., Sato, T., Nozawa, S., Kim, K. H., Lee, J. H., Choi, J., Tomita, A., Ichikawa, H., Adachi, S., Ihee, H. & Koshihara, S. (2009). *J. Synchrotron Rad.* **16**, 391–394.

Ichiyanagi, K., Takagi, S., Kawai, N., Fukaya, R., Nozawa, S., Nakamura, K. G., Liss, K. D., Kimura, M. & Adachi, S. (2019). *Sci. Rep.* **9**, 7604.

Kalantar, D. H., Belak, J. F., Collins, G. W., Colvin, J. D., Davies, H. M., Eggert, J. H., Germann, T. C., Hawreliak, J., Holian, B. L., Kadau, K., Lomdahl, P. S., Lorenzana, H. E., Meyers, M. A., Rosolankova, K., Schneider, M. S., Sheppard, J., Stölken, J. S. & Wark, J. S. (2005). *Phys. Rev. Lett.* **95**, 075502.

Kraus, D., Vorberger, J., Pak, A., Hartley, N. J., Fletcher, L. B., Frydrych, S., Galtier, E., Gamboa, E. J., Gericke, D. O., Glenzer, S. H., Granados, E., MacDonald, M. J., MacKinnon, A. J., McBride, E. E., Nam, I., Neumayer, P., Roth, M., Saunders, A. M., Schuster, A. K., Sun, P., van Driel, T., Döppner, T. & Falcone, R. W. (2017). *Nat. Astron.* **1**, 606–611.

Lutterotti, L., Matthies, S. & Wenk, H.-R. (1999*a*). *IUCr Commission on Powder Diffraction Newsletter*. No. 21, pp. 14–15.

Lutterotti, L., Matthies, S. & Wenk, H.-R. (1999*b*). *Proceeding of the 12th International Conference on Textures of Materials (ICOTOM-12)*, pp. 1599–1604. Ottawa: NRC Research Press.

McQueen, R. G., Marsh, S. P. & Fritz, J. N. (1967). *J. Geophys. Res.* **72**, 4999–5036.

Meyers, M. A., Gregori, F., Kad, B. K., Schneider, M. S., Kalantar, D. H., Remington, B. A., Ravichandran, G., Boehly, T. & Wark, J. S. (2003). *Acta Mater.* **51**, 1211–1228.

Milathianaki, D., Boutet, S., Williams, G. J., Higginbotham, A., Ratner, D., Gleason, A. E., Messerschmidt, M., Seibert, M. M., Swift, D. C., Hering, P., Robinson, J., White, W. E. & Wark, J. S. (2013). *Science*, **342**, 220–223.

Mitchell, A. C. & Nellis, W. J. (1981). *J. Appl. Phys.* **52**, 3363–3374.

Nellis, W. J., Moriarty, J. A., Mitchell, A. C., Ross, M., Dandrea, R. G., Ashcroft, N. W., Holmes, N. C. & Gathers, G. R. (1988). *Phys. Rev. Lett.* **60**, 1414–1417.

Niwa, Y., Sato, T., Ichiyanagi, K., Takahashi, K. & Kimura, M. (2016). *High. Press. Res.* **36**, 471–478.

Nozawa, S., Adachi, S., Takahashi, J., Tazaki, R., Guérin, L., Daimon, M., Tomita, A., Sato, T., Chollet, M., Collet, E., Cailleau, H., Yamamoto, S., Tsuchiya, K., Shioya, T., Sasaki, H., Mori, T., Ichiyanagi, K., Sawa, H., Kawata, H. & Koshihara, S. (2007). *J. Synchrotron Rad.* **14**, 313–319.

Rygg, J. R., Eggert, J. H., Lazicki, A. E., Coppari, F., Hawreliak, J. A., Hicks, D. G., Smith, R. F., Sorce, C. M., Uphaus, T. M., Yaakobi, B. & Collins, G. W. (2012). *Rev. Sci. Instrum.* **83**, 113904.

Sliwa, M., McGonegle, D., Wehrenberg, C., Bolme, C. A., Heighway, P. G., Higginbotham, A., Lazicki, A., Lee, H. J., Nagler, B., Park, H. S., Rudd, R. E., Suggit, M. J., Swift, D., Tavella, F., Zepeda-Ruiz, L., Remington, B. A. & Wark, J. S. (2018). *Phys. Rev. Lett.* **120**, 265502.

Suggit, M., Kimminau, G., Hawreliak, J., Remington, B., Park, N. & Wark, J. (2010). *Rev. Sci. Instrum.* **81**, 083902.

Suggit, M. J., Higginbotham, A., Hawreliak, J. A., Mogni, G., Kimminau, G., Dunne, P., Comley, A. J., Park, N., Remington, B. A. & Wark, J. S. (2012). *Nat. Commun.* **3**, 1224.

Swegle, J. W. & Grady, D. E. (1985). *J. Appl. Phys.* **58**, 692–701.

Torchio, R., Occelli, F., Mathon, O., Sollier, A., Lescoute, E., Videau, L., Vinci, T., Benuzzi-Mounaix, A., Headspith, J., Helsby, W., Bland, S., Eakins, D., Chapman, D., Pascarelli, S. & Loubeyre, P. (2016). *Sci. Rep.* **6**, 26402.
Tracy, S. J., Turneaure, S. J. & Duffy, T. S. (2018). *Phys. Rev. Lett.* **120**, 135702.
Turneaure, S. J., Renganathan, P., Winey, J. M. & Gupta, Y. M. (2018). *Phys. Rev. Lett.* **120**, 265503.
Wehrenberg, C. E., McGonegle, D., Bolme, C., Higginbotham, A., Lazicki, A., Lee, H. J., Nagler, B., Park, H. S., Remington, B. A., Rudd, R. E., Sliwa, M., Suggit, M., Swift, D., Tavella, F., Zepeda-Ruiz, L. & Wark, J. S. (2017). *Nature*, **550**, 496–499.
Wenk, H.-R., Matthies, S., Donovan, J. & Chateigner, D. (1998). *J. Appl. Cryst.* **31**, 262–269.
Whitley, V. H., McGrane, S. D., Eakins, D. E., Bolme, C. A., Moore, D. S. & Bingert, J. F. (2011). *J. Appl. Phys.* **109**, 013505.